CrossMark
← click for updates

Ultrafast direct fabrication of flexible substrate-supported designer plasmonic nanoarrays†

Yaowu Hu,[a,b] Prashant Kumar,[a,b,c] Rong Xu,[d] Kejie Zhao[d] and Gary J. Cheng*[a,b,d]

Fabrication of plasmonic nanostructures has been an important topic for their potential applications in photonic and opto-electronic devices. Among plasmonic materials, gold is one of the most promising materials due to its low ohmic loss at optical frequencies and high oxidation resistance. However, there are two major bottlenecks for its industrial applications: (1) the need for large-scale fabrication technology for high-precision plasmonic nanostructures; and (2) the need to integrate the plasmonic nanostructures on various substrates. While conventional top-down approaches involve high cost and give low throughput, bottom-up approaches suffer from irreproducibility and low precision. Herein, we report laser shock induced direct imprinting of large-area plasmonic nanostructures from physical vapor deposited (PVD) gold thin film on a flexible commercial free-standing aluminum foil. Among the important characteristics of the laser-shock direct imprinting is their unique capabilities to reproducibly deliver designer plasmonic nanostructures with extreme precision and in an ultrafast manner. Excellent size tunability (from several μm down to 15 nm) has been achieved by varying mold dimensions and laser parameters. The physical mechanism of the hybrid film imprinting is elaborated by finite element modeling. A mechanical robustness test of the hybrid film validates a significantly improved interfacial contact between gold arrays and the underlying substrate. The strong optical field enhancement was realized in the large-area fabricated engineered gold nanostructures. Low concentration molecular sensing was investigated employing the fabricated structures as surface-enhanced Raman scattering (SERS) substrates. The ability to ultrafast direct imprint plasmonic nanoarrays on a flexible substrate at multiscale is a critical step towards roll-to-roll manufacturing of multi-functional devices which is poised to inspire several emerging applications.

1. Introduction

Designer gold arrays, representing ordered gold structures fabricated according to one's design, have attracted tremendous interest due to their unprecedented ability in electromagnetic field confinement and potential applications in a vast array of photonics and optoelectronics technologies,[1–3] ranging from chemical and biosensing[4–6] to energy harvesting,[7] imaging,[8,9] data storage[10–12] and optical tweezers for nanomaterials manipulation.[13–16] Gold is the most commonly used material in plasmonic and optical metamaterial devices due to its chemical stability and small ohmic losses at optical frequencies. While its use in basic research keeps growing, the commercialization and practical implementations of laboratory research to benefit the society have been greatly hindered by high cost and low throughput inherited in current fabrication techniques.[17–19] For example, bottom-up approaches such as guided growth and self-assembly suffer from poor control, reproducibility and scalability.[20–23] Top-down techniques such as the conventional lithography process[24–26] followed by metallization and lift-off involve multiple steps and usually require high standard cleanrooms, which need significant capital and energy investment. Furthermore, the conventional techniques have exclusively been limited to flat surfaces. Exploring approaches to achieve gold arrays on flexible substrates could bring advantages from their capability to wrap around non-planar surfaces and combine with next generation flexible electronic devices with multiple functions.

Several methods have been developed to enable large-scale precise patterning in a relatively rapid and low-cost fashion. Nanoimprint lithography[27–30] has been a commonly employed approach for mechanically deforming photoresists or polymers followed by curing at elevated temperatures or ultraviolet light illumination; however, subsequent etching of the residual polymer, metal deposition and lift-off are still the required

[a]*School of Industrial Engineering, Purdue University, West Lafayette, Indiana, USA-47907. E-mail: gjcheng@purdue.edu*
[b]*Birck Nanotechnology Center, Purdue University, West Lafayette, Indiana, USA-47907*
[c]*Department of Physics, Indian Institute of Technology Patna, Bihta, India-801103*
[d]*School of Mechanical Engineering, Purdue University, West Lafayette, Indiana, USA-47907*

steps to generate the final metallic arrays, sophisticating the process. Template stripping[31–34] has been used to obtain smooth metallic structures on flexible substrates over wafer-scale areas by thermal annealing of a polymer substrate and a silicon mold with metal layers sandwiched in between, yet it lacks the capability of roll-to-roll manufacturing. Thermo-plastic forming of bulk metallic glasses[35,36] by taking advantage of temperature dependence of material strength would generate geometrical inaccuracies due to thermal expansion and capillary action. Consequently, the development of a novel technique capable of high-throughput and precise direct fabrication of multiscale gold arrays on a flexible substrate is of great importance for next-generation devices and is expected to be useful for various potential emerging applications.

In this article, we develop laser shock multi-layer imprint-ing (LSI) to realize ultrafast and precise fabrication of flexible substrate-supported gold arrays. In this approach, the thin gold coating is supported on a free-standing aluminum foil because of its availability at the commercial scale and good formability. Ultrahigh shock pressure is generated by laser ablation of graphite[37–39] to deform the multi-layered film against a silicon mold. To gain insight into the underlying phenomena in LSI of the hybrid, a finite element model (FEM) is developed to study the transient stress and temperature fields. Structural integrity of the hybrid material system is tested to evaluate its mechanical robustness. The capability of optical field confinement of the patterned gold arrays is investigated by employing them as surface enhanced Raman scattering (SERS) substrates for sensitive molecular detection.

2. Materials and methods

Fig. 1(a) shows the silicon mold with various dimensions fabricated by electron-beam lithography and dry/wet etching. The experimental set-up to achieve precision multiscale patterned metallic structures by LSI is shown in Fig. 1(c). A Q-switch Nd-YAG laser (Continuum® Surelite III) (1064 nm wavelength and 5 ns pulse duration) was used to irradiate a sacrificial layer with graphite coating (Asbury Carbons, USA) sprayed on a 4 μm thick Al foil (Lebow Company, USA). A fused silica was placed on top of the graphite coating to confine and enhance plasma expansion. Intense laser fluence instantaneously evaporated the graphite layer and ionized plasma and strong momentum was generated. The shock wave was then transferred onto the target sample which sits directly on the fabricated micro-/nano-scale silicon mold. The dimension of the sample is around 10 mm × 10 mm. The diameter of the laser beam is controlled by a focus lens and measured by using a photosensitive paper. The typical diameter used is 3 mm. A motorized XY stage was used to achieve in-plane translation of the sample for laser scanning. Deformation depths were closely monitored with the variation of single pulse laser intensity and trench width. Trench molds of various trench widths from 4 μm and down to 15 nm were used in the present experimental investigations. Laser intensities up to 0.7 GW cm^{-2}

(measured by using Newport 1916c power meter) were applied to investigate laser shock imprinting of micro/nano-patterns. The target material is composed of a gold layer and a flexible substrate. In this study, a 4 μm thick aluminum foil was used as the flexible handling substrate. The foil was cleaned by toluene, acetone, and isopropyl alcohol successively for 5 minutes. After it was dried naturally , the sample was mounted on a holder in order to coat a gold layer. The above mentioned laser shock processing was applied to achieve micro/nano-imprinting. The resultant imprinted film after peel off from the micro/nano-mold had inverted structures. Besides gold, other plasmonic materials (such as silver or copper) which exhibit plastic formability under laser shock induced high-strain-rate deformation could also be coated and processed. A Au film of thickness 100 nm or 200 nm was de-posited onto the flexible aluminum foil by electron beam deposition at a rate of 1 nm s^{-1}. An ultra-thin titanium layer (∼5 nm) is used as the adhesion layer. Al foil can be replaced by flexible polymers as well, as the heat generated during nanosecond laser ablation is with a small dissipation length (within 500 nm) and it would thus not affect the substrate. The target film is kept in a dry environment and cut into smaller pieces for each usage. No further gold coating is needed before its exhaustion.

The mechanical properties of the laser shock processed hybrid film were evaluated from the penetration force–displacement curves obtained from nanoindentation tests using a Keysight Nano-Indenter G200 with a standard Berkovich diamond indenter. Three kinds of indentation tests were performed during the experiment: indentations on the untreated, treated flat, and the treated curve surface of the samples. To evaluate the mechanical properties along the thickness, tests were performed under force control with several loading/unloading cycles. The loading time and the hold period at maximum displacement were 10 s and 2 s, respectively. Afterwards, the indenter was withdrawn at the same rate as during the loading cycle. From these tests, mechanical properties like hardness and elastic modulus can directly be obtained from force–displacement curves by the standard Oliver and Pharr method.[40]

A coupled temperature displacement dynamic FEM model was developed to simulate stress and temperature fields. The analysis type was assigned to be plane strain. The element type used is CPE4RT which features 4-node bilinear displacement and temperature, reduced integration and hourglass control. Molecular dynamics simulation of the indenter–structure interaction is carried out to illustrate the influence of interfacial discontinuities on integrated mechanical response of the hybrid film. An embedded atom method (EAM) potential with improved force matching methodology[41] and FCC (face-centered cubic) structures was used for gold and aluminum. A constant force of 0.05 eV Å^{-1} was applied to the indenter. Lennard-Jones (LJ) potential was used to describe the van der Waals interaction between gold and the mold. The calculation was performed in a microcanonical (NVE) ensemble around 300 K. The time step was 1 fs. Molecular detection capability
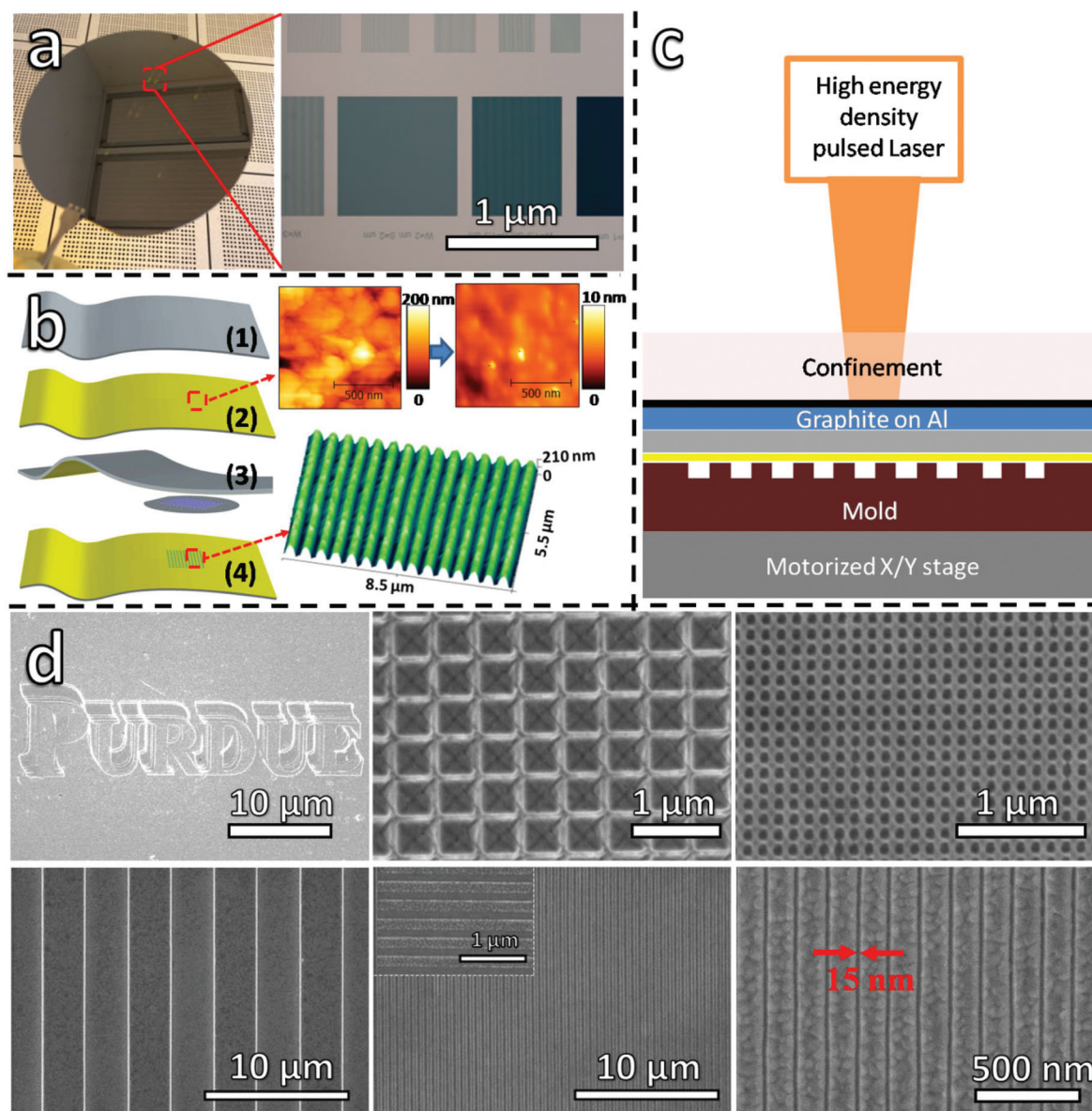
Fig. 1 (a) Optical images of fabricated silicon mold. Scale bar: 1 mm. (b) Processing procedures for patterning 3D structures on the hybrid film: (1) initial film; (2) deposition of a thin layer of functional material; (3) LSI process; (4) final film. Inserted are AFM images of gold coated flexible foil before laser shock, flat and structured areas after laser shock respectively. (c) Schematic drawing of LSI forming. (d) SEM images of obtained structures. Inserted is higher resolution SEM image of nanostructure.

was demonstrated by soaking the fabricated sample in diluted rhodamine 6G aqueous solution for 30 min followed by thoroughly cleaning with de-ionized water. Raman instruments with laser wavelengths of 633 nm and power 0.25 mW were used to record the Raman fingerprints of the molecules.

3.   Results and discussion

Micro- and nanometer scale gold patterns are fabricated precisely and reproducibly, as shown in the FESEM images in Fig. 1(d). The present LSI technique is equipped with the capa-

bility of precision nanoscale imprinting of functional nanostructures on flexible substrates in a scalable and reproducible manner. Structures including but not limited to trenches, circles, and holes with dimensions as low as 20 nm have been obtained on the hybrid film by a single laser shock. Deposition of a layer of Au on a thin flexible substrate generally results in much rougher surfaces, because of the thermal stress and deformation associated with the rapid non-uniform heating and cooling effect during the deposition process, large initial roughness of the supporting substrate, and wrinkles generated during sample cleaning and handling. As shown in Fig. 1(b), the measured surface height variation of the deposited gold

film on aluminum foil is around 200 nm, which is more than 10 times larger than the usual surface roughness reported for rigid substrates. However, as the gold surface is placed against an atomically smooth silicon mold, upon laser shock processing, the ultra-high shock pressure generated during plasma expansion instantaneously flattens the gold surface, resulting in a much smoother surface with the measured surface height variation ~10 nm, which is 20 times better than that without laser processing and the surface smoothness is comparable to the features attained on a rigid silicon substrate. The flattening effect arises from the plastic flow of gold and the underlying substrate under laser shock pressure. Thus, LSI exhibits superior performance as compared to other existing imprinting technologies, as far as surface smoothness of the fabricated features is concerned.

The deformation depth of micro/nanoscale features attained by the LSI process is observed to be closely related to the laser intensity and geometrical parameters of the mold. For a fixed trench width, higher laser power used for the purpose of forming, results in deeper trenches. Strong laser power dependence of deformation depth is visualized by approximately three-fold rise in the deformation depth when the laser intensity is increased from 0.1 to 0.4 GW cm^{-2}. Apparently, there is a threshold of laser intensity, over which one attains good formability. Typically, nanoscale features require a larger laser pressure to be deformed conformally, compared to the micro or millimeter scale features. To ensure a high fidelity feature transfer for all structures with a single laser shock, an intensity of 0.7 GW cm^{-2} is thus used.

3.1 Deformation mechanism of gold arrays by LSI

To gain insight into the hybrid film shock forming process, a simplified model implemented by FEM is developed to illustrate the stress and temperature fields with the advance of time.

A simplified model for laser induced shock momentum is given in ref. 44–49,

$$\frac{dL(t)}{dt} = \frac{2}{Z}P(t) \tag{1}$$

$$I(t) = P(t)\frac{dL(t)}{dt} + \frac{3}{2\alpha}\frac{d}{dt}[P(t)L(t)] \tag{2}$$

where $P(t)$ is the laser induced shock pressure at a given instant, $I(t)$ is the effective laser intensity at time t, and $L(t)$ is the thickness of the interface at time t. α is a constant to represent a fraction of internal energy related to pressure. Z is the shock impedance given in ref. 50,

$$\frac{2}{Z} = \frac{1}{Z_1} + \frac{1}{Z_2} \tag{3}$$

where Z_1 and Z_2 are the impedances for the target metal and the confining media, respectively.

The impulse imparted by the shock waves raises the momentum of the metal thin film to a level which suffices for the 3D plastic deformation conformal to the micro/nanoscale molds. Metals under extreme laser shock pressure, achieve

excellent 3D micro/nano forming due to the high strain rate exceeding 10^6 s^{-1}. Ultrafast laser based 3D micro/nano forming results in compactness in formed materials which strengthens them. Since the strain rate varies over a huge range within a minute fraction of second, plastic strain σ would have significant strain rate dependence. Considering that the Johnson–Cook (J–C) strain sensitive plasticity model applies to the present case, the slope of the flow stress curve is independently influenced by strain, the dimensionless strain rate and local temperature achieved in constriction.

$$\sigma = (A + B\varepsilon^n)\left(1 + C\ln\frac{\dot{\varepsilon}}{\dot{\varepsilon}_0}\right)(1 - T^{*m}) \tag{4}$$

where ε is the plastic strain, $\dot{\varepsilon}$ is the plastic strain rate, and $\dot{\varepsilon}_0$ is the reference strain rate. A, B, and C are material constants. T^* is the homologous temperature defined by,

$$T^* = \frac{T - T_r}{T_m - T_r} \tag{5}$$

where T_r is the transition temperature and T_m is the temperature at which melting occurs.

Temperature rise during the high strain rate process is considered by setting the inelastic heat fraction for plastic flow. The temperature dependence of yield stress is set to zero, as it was found that the yield stress of gold does not vary with temperature in the low temperature region.[52] Two different sets of thermal and mechanical properties are assigned to represent the deposited polycrystalline Au layer and aluminum. ABAQUS software has been used to numerically simulate the stress as well as the temperature fields during the process. The mechanical and thermal properties of aluminum and gold are shown in Table 1.

Fig. 2(a) shows the successive stages of hybrid film deformation under shock pressure. At abrupt geometrical changes, materials are subjected to severe strain fields due to stress concentration. For different laser conditions, the calculated von Mises stress fields and cross sections are different, as shown in Fig. 2(b and c). The stress field in gold coating is generally larger than that in aluminum because of its stronger strain-rate sensitivity (Table 2). At the upper corner of the mold, the Au layer directly bears the reaction force from the mold and flows into the trench. The thickness of the Au layer inside the trench is thus anticipated to be thicker than that outside (Fig. 2(c, e and g)). Depending on the stage of the deformation and laser intensity, the Au layer can suspend on the trench (Fig. 2(b, d and f)) for low laser shock pressure, or touch the

Table 1 Mechanical and thermal properties of aluminum and gold[42,43]

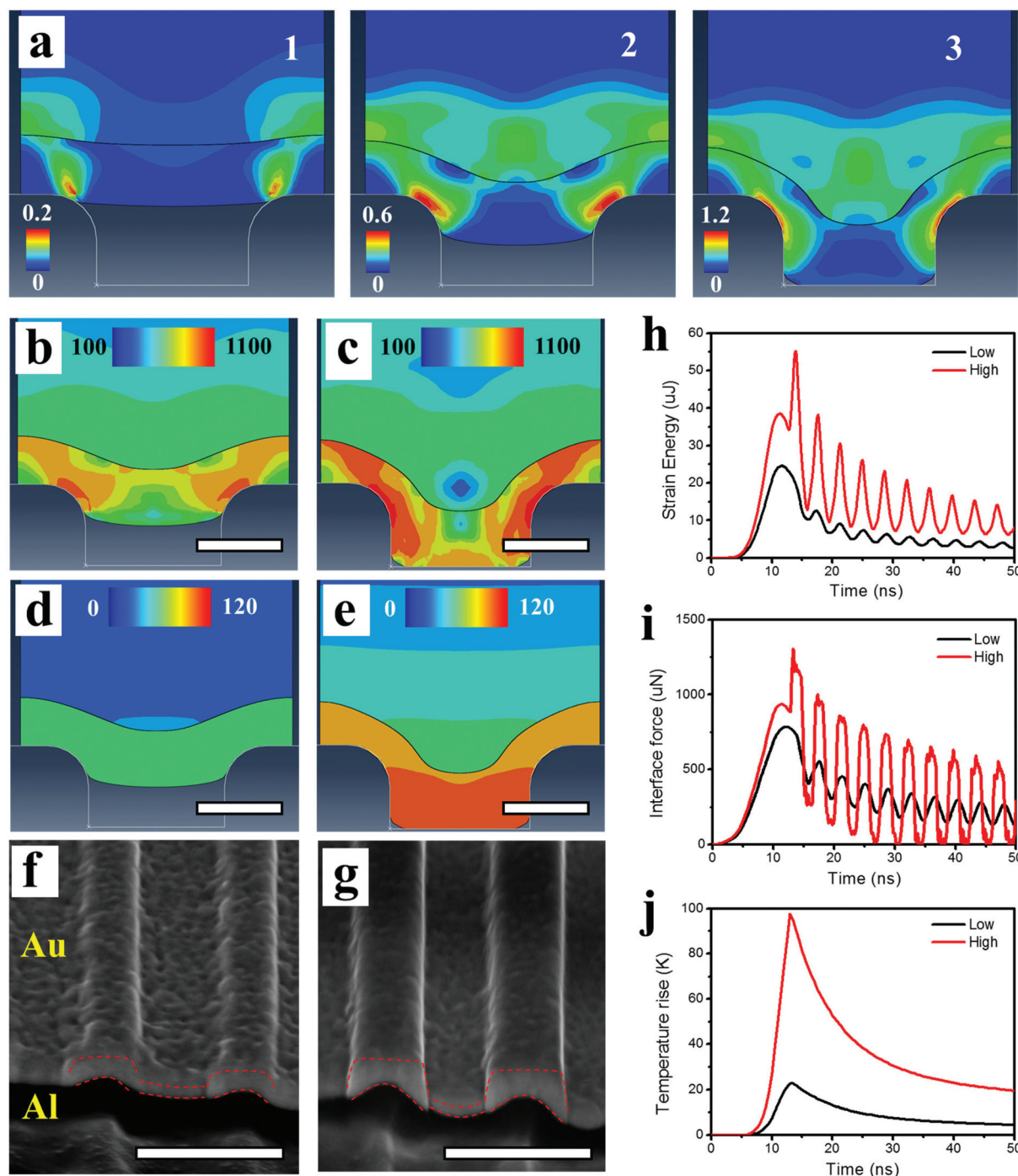|	Al	Au
Density (g cm^{-3})	2.7	19.3
Young's modulus (GPa)	36	79
Poisson ratio	0.33	0.42
Thermal conductivity (Wm^{-1} K^{-1})	237	318
Specific heat capacity (J g^{-1} °C^{-1})	0.90	0.16
Coefficient of thermal expansion (K^{-1})	14.2×10^{-6}	23.1×10^{-6}
Melting temperature (°C)	660	1064

Fig. 2 (a) Schematic of plastic strain generation during laser shock imprinting of hybrid films with different mechanical properties: (1) initialization of plastic flow, (2) developed stage, (3) final stage. Laser intensity: 0.48 GW cm^{-2}. (b−e) Calculated von Mises stress fields (unit: MPa) (b−c) and temperature fields (unit: K) (d−e) for laser intensities of 0.27 GW cm^{-2} (b, d) and 0.48 GW cm^{-2} (c, e), respectively. (f−g) Corresponding FESEM images of obtained cross-sections. Scale bars: (a−e) 300 nm, (f−g) 1 μm. (h) Strain Energy history of the system. (i) Corresponding contact force at gold coating and aluminum film interface. (j) Temperature rise and dissipation due to high strain rate deformation and thermal transport.

bottom (Fig. 2(c, e and g)) for high laser shock pressure. The gold layer under high shock pressure is punched against the ultra-flat silicon mold, thus generating a replicated smooth surface. The simulated results in Fig. 2(b−e) qualitatively agree well with those from experiments (Fig. 2(f−g)).

Fig. 2(h) shows the strain energy of the hybrid during and after laser shock loading. While the pulse duration is only 5 ns, the first peak in strain energy is found to occur several nanoseconds later than the peak in laser intensity, which resulted from the prolonged plasma-induced shock pressure

Table 2 Parameters for Johnson–Cook plastic model[43,51,52] for Al and Au with an average grain size around 80 nm

	A (MPa)	B (MPa)	C	n	T_r (°C)	m
Al	140	157	0.016	0.167	527	1.7
Au	120	243	0.056	0.147	23	0

due to confining media and a time delay for elastic and plastic stress wave propagation. The second peak, which is more obviously present in the case of high laser intensity, emerges when the film impacts on the bottom of the mold and kinetic energy of the material transfers into strain energy of the system. Similar phenomena are found for the interface force (Fig. 2(i)). The strain energy, interface force and local temperature rise (Fig. 2(j)) are found to decay as plastic stress wave propagates and reflects. The maximum temperature rise is around 100 K and 20 K for laser intensity of 0.48 GW cm^{-2} and 0.27 GW cm^{-2}, respectively. Thermal energy is uniform inside the thin gold layer and dissipates quickly due to the high thermal conductivities of the metals. Depending on the material properties, maximum temperature which locally rises in the ultra-high strain rate deforming process could be increased, due to the competing effects of heat generation and dissipation. It should be noted that accurate material properties and processing parameters are often difficult to obtain, especially in the present case of non-equilibrium plasma shock induced micro/nanoscale high-strain-rate deformation. However, the calculated results shown in Fig. 2 could be interpreted qualitatively and serve as estimations of temperature rise and deformation profile.

3.2 Mechanical robustness of metal-flexible substrate interfaces

Extreme laser pressure burst in confined geometries is poised to elevate local temperature at sharp corners. However, since the laser pulse does not last longer than a few nanoseconds, diffusion of heat will be fast and hence laser shock processing provides a technological platform for relatively cold nanoforming which will have immense capabilities. Unlike the hot forming techniques, LSI is a cold forming process which provides an extremely high strain rate, resulting in high formability of metals and ultrasmooth nanoscale surface features. Metals pushed into the mold cavity with laser shock pressure experience severe plastic deformation and nanocrystallization around the corner of the nanomolds, followed by dynamic crystallization in the mold cavity. As a result, the mechanical properties of the imprinted metal are enhanced, as shown in the hardness values obtained from nanoindentation (Fig. 3(a)). As the hybrid film gets deformed into 3D shapes, the surface profile, local stress–strain and temperature history would greatly impact the surface hardness. Thus variations of surface hardness after shock pressure were expected. It was also found that the surface hardness of LSI samples increases with increasing laser intensity, due to dislocation, multiplication

and strain hardening. Due to spatial variations of material thickness, local temperatures and strain histories, the measured hardness at different locations varies, as listed in Table 4. On the top of the structures, the hardness is found to be the highest, followed by the bottom, and then the unstructured areas. This agrees with experimental and simulated cross-section profiles in Fig. 2(b–g), with a thicker gold layer inside the trench. For all samples treated by LSI, the hardness has a decreasing trend as the tip indents into the surface, due to the strong surface effect of LSI and the size effect during indenter–surface interaction.[53,54]

For gold nanoarrays supported on flexible substrates, sufficient interfacial strength is needed for practical applications. Fig. 3(b) shows the obtained cross-sections of the hybrid film before LSI. The interface between Au and Al is distinct and loose before LSI, which might result in Au layer peeloff when the hybrid foil is bent. After LSI, a significant interface improvement is observed. As shown in Fig. 3(c), it is found that Au and Al atoms diffuse into the adjacent layers, overcoming surface imperfections such as an oxide layer, adsorbed molecules and contaminations. In order to study the influence of shock pressure on the integrated mechanical properties of the hybrid film, the load-displacement curves were monitored on these samples during nanoindentation. As shown in Fig. 3(d) for the untreated sample, large discontinuities are observed at loads between 0.2 mN and 0.4 mN, or at penetration depths between 50 nm and 150 nm, for all 50 randomly selected locations on films before LSI. The jumps of displacement during indentation are between 45 nm and 140 nm. This sudden displacement jump, known as a "pop-in" effect, was previously observed during indenting of single-crystalline metals, semiconductors, and ionic crystals, and was believed to be the transition from pure elastic to plastic deformation as a result of homogeneous defect generation.[55–57] However, as shown in the surface morphology of the indented area (Fig. 3(a)), the test generated a pyramid indent on the surface with no observable surface cracks, eliminating the possibility of brittle failures. Large plastic deformation before pop-in is also clearly shown from the differences in the loading and unloading curves shown in Fig. 3(d). Thus "pop-in" in the present study should be attributed to the loose contact at the internal interface, grain boundary sliding of the multi-crystalline gold coating, and large surface roughness. As listed in Table 3, LSI could effectively diminish the probability of occurrence of "pop-in". The displacement jump length is largely shortened by LSI. The occurrence depth and force are both decreased upon laser shock, indicating better layer-to-layer contacts and improved surface morphology. The suppression of the pop-in effect is a clear evidence of enhancing mechanical properties by LSI. To address the influence of interfacial strength on indenter–multilayered film interaction, molecular dynamics simulations with and without an interface void was carried out as shown in Fig. 3(e–h). By comparing Fig. 3(f) and (h), the triangular indenter under constant loading is found to have a higher velocity when it penetrates to the proximity of the interfacial discontinuities due to void-induced stress-redistri-
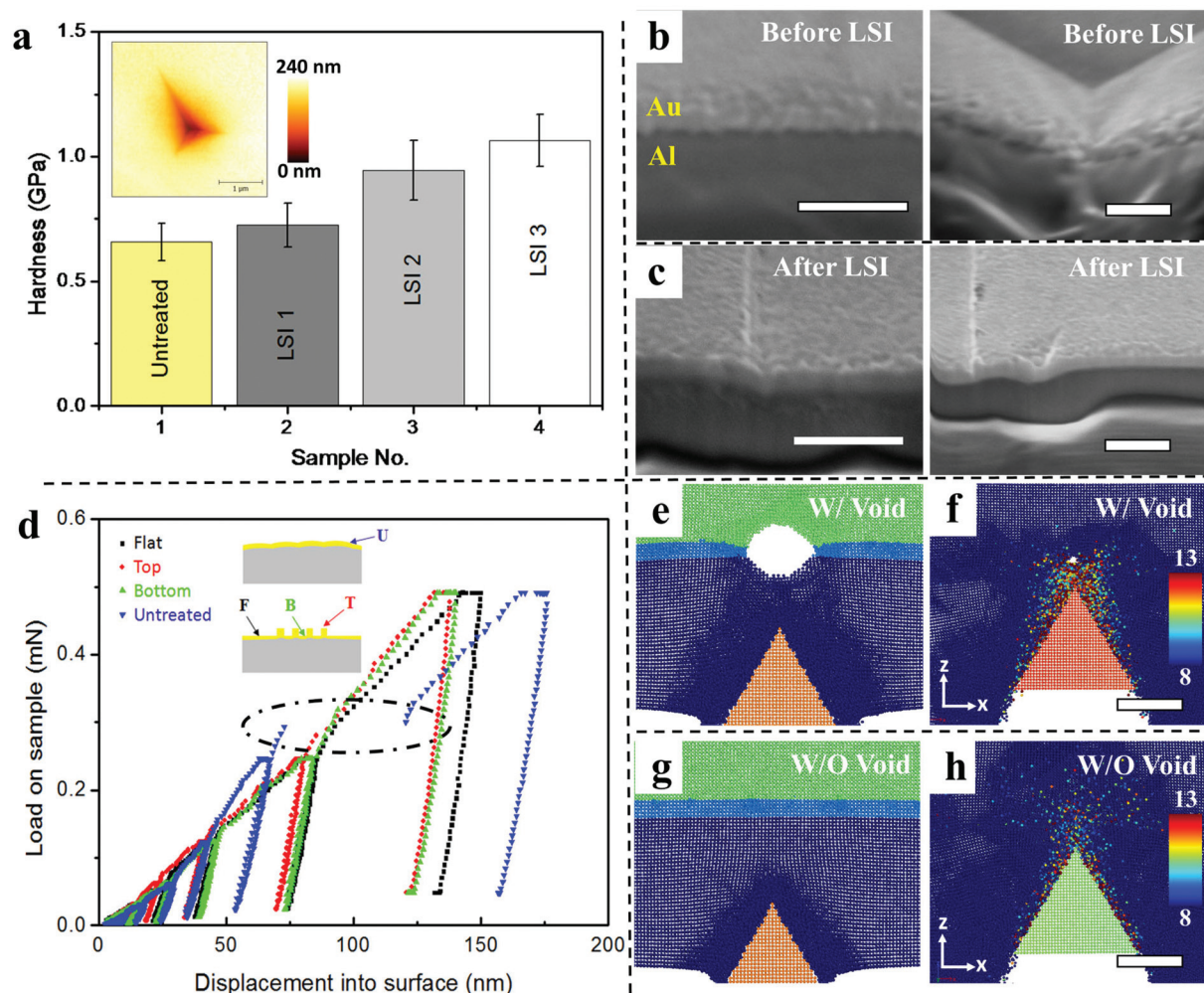
Fig. 3 Enhanced mechanical properties by laser shock. (a) Experimentally obtained hardness values of untreated, shock imprinted samples with various laser intensities (LSI 1: 0.07 GW cm^{-2}, LSI 2: 0.27 GW cm^{-2}, LSI 3: 0.48 GW cm^{-2}, loading force: 0.5 mN). Inset: typical AFM image of indented surface. (b–c) FESEM imaging of surface morphologies for untreated samples (b) showing sharp interface edges, and LSI treated samples (c). Scale bars: 1 μm. (d) Load-displacement curves obtained on samples before LSI treatment ("pop-in"), and at various locations on generated structures after LSI. Laser intensity: 0.48 GW cm^{-2}. (e–h) Schematic of molecular dynamics simulations (e, g) and calculated velocity (z-direction, unit: Å fs^{-1}) fields (f, h) at 11 picosecond in nanoindentation of multi-layered films with (e–f) and without (g–h) interface discontinuities. Scale bars (f, h): 4 nm.

Table 3 Pop-in event probability, length of displacement jump, occurrence depth and force variations with laser intensity

Laser intensity (GW cm^{-2})	Probability of pop-in (%)	Length of displacement jump (nm)	Occurrence depth (nm)	Occurrence force (mN)
0	100	45	73	0.31
0.07	53	12	55	0.2
0.27	0	0	NA	NA
0.48	0	0	NA	NA

Table 4 Calculated hardness values

Load (μN)	Hardness (GPa)			
	Flat	Top	Bottom	Untreated
0.125	1.67	2.05	1.77	1.92
0.25	1.32	1.46	1.31	2.07
0.5	0.92	1.07	1.04	0.47

bution and subsequent collapsing, giving rise to the experimentally observed load-displacement jump. LSI could effectively densify porous thin-films, facilitate interlayer atom diffusion and introduce enhanced integration of multi-layered structures, thus preventing the aforementioned "pop-in" on LSI treated samples and resulting in mechanically robust multi-layered thin films.

The idea behind coating a functional plasmonic gold layer on the top of a flexible aluminum layer was to take

advantage of the excellent formability of aluminum and at the same time it would minimize the product cost by a huge margin. Mechanical properties studied by nanoindentation experiments indicate excellent structural integrity of the hybrid as forming is carried out by laser shock pressure.

High strain rate processing, excellent heat dissipation and interfacial interactions are held responsible for enhanced mechanical robustness of the formed nanoscale features which ultimately provides fidelity which is needed for precision nanomanufacturing.
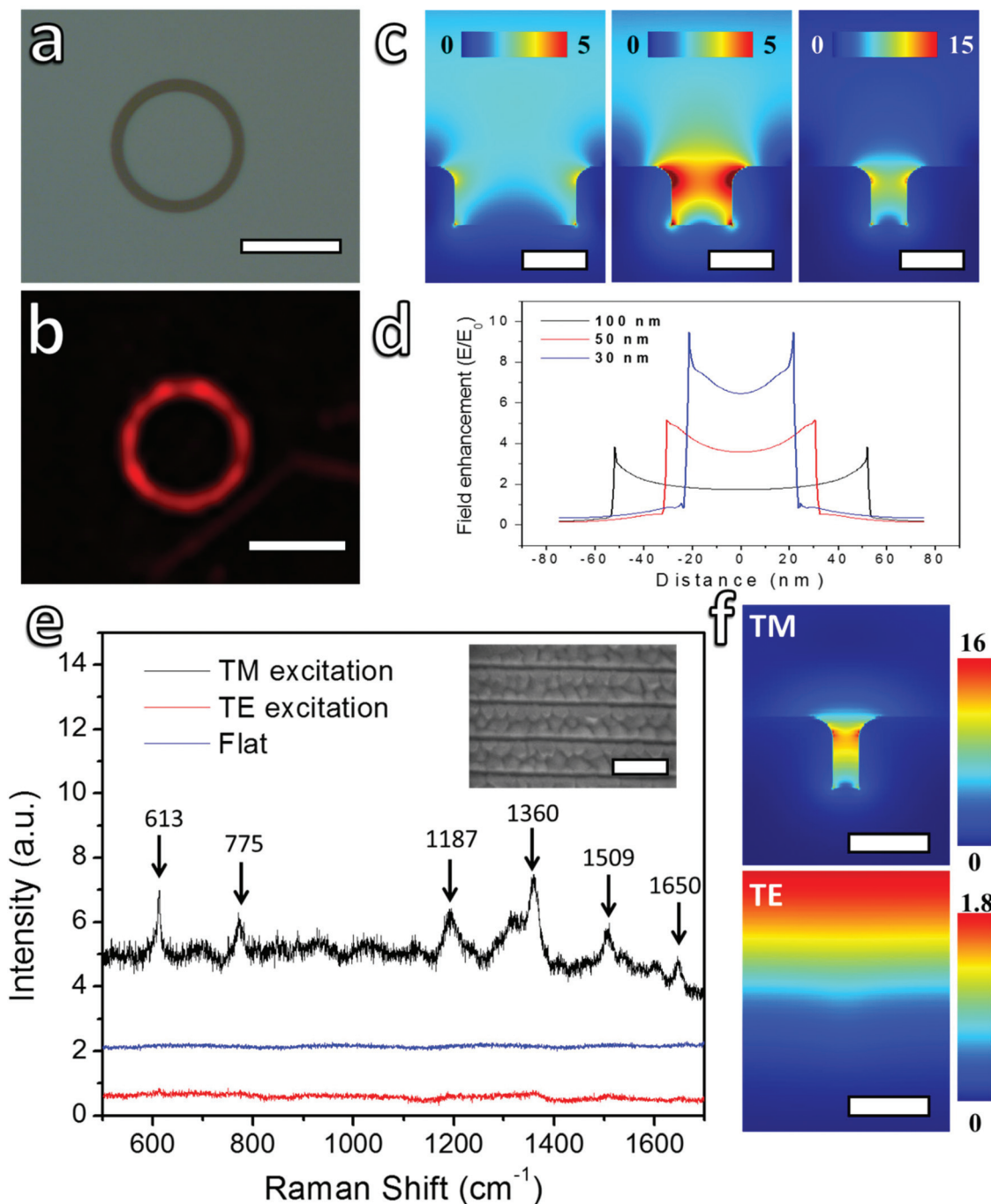

Fig. 4 Field confinement of fabricated flexible gold arrays. (a) Optical image of a circle with nanostructures for LSI. Scale bar: 50 μm. (b) Confocal Raman mapping of obtained circle consisting of Au nanoarrays. Scale bar: 50 μm. (c) FDTD simulations of trenches between two slits with different slit width (100 nm, 50 nm and 30 nm). Structures are with depths of 50 nm and with periods of 150 nm. Scale bars: 50 nm. (d) Line profiles of obtained field enhancements in (c). (e) Raman spectra of R6G molecules on flat and patterned gold coated aluminum film, inserted is the SEM image of the slit arrays (pitch: 150 nm; slit width: 15 nm; depth: 50 nm). Scale bar: 150 nm. (f) Calculated local field under transverse magnetic (TM) mode and transverse electric (TE) mode illuminations with incident light λ = 633 nm and mesh size 0.5 nm. Scale bars: 50 nm.

3.3 Molecular sensing by fabricated hybrid SERS platform

Plasmonic gold coating when nanopatterned, bear significance due to their capability of focusing light at one's will. The structural dimensions of the generated pattern define the local electric field when light is incident upon them. LSI is spatially selective in the ultrafast fabrication of multiscale designed patterns consisting of gold nanostructures, as shown in Fig. 4(a and b). By adjusting the structural dimensions, different field enhancements could be generated (Fig. 4(c and d)). In general, by reducing the slit width of the nanostructures, higher field confinements could be achieved according to our FDTD simulations shown in Fig. 4(d). To experimentally demonstrate the field enhancement capability, molecular sensing of 70 nM Rhodamine 6G (R6G) (Sigma Aldrich) was tested. The laser power is kept low while spectral recording was being carried out, in order to avoid apparent temperature rise of the samples which possibly can photocarbonize the R6G molecules. The molecules are off resonance at 633 nm red laser excitation, so that the detected signals could be attributed to field enhancement. As shown in Fig. 4(e), under transverse magnetic (TM) mode excitation, the luminescence background of Au is found to be hugely increased after laser shock patterning of the Au film into a nanoscale trench. The vibrational fingerprints of the molecules at 613, 775, 1187, 1360, 1509 and 1650 cm^{-1} could clearly be distinguished when molecules are anchored by the Au trenches, which is of significant difference as compared to the background Raman spectrum recorded for the flat Au surface. Such distinctions of Raman peaks are due to the local electric field evolved under incident light. The optical field enhancements under laser illumination are also shown in our FDTD simulations in Fig. 4(f). Few/single molecule detection could be carried out in future by designing more complex structures, optimizing the geometrical dimensions and shifting the plasmonic resonance wavelength to the resonant frequency of molecules to be diagnosed. For the surface-enhanced Raman scattering (SERS) effect from an ordered array with deterministic hot spot intensities and locations, our result is apparently higher than that reported by Zhu *et al.*[58] where a much higher molecular concentration of R6G was used onto gold-void nanostructures fabricated by the self-assembly assisted electrochemical deposition process under a molecular resonance frequency. It should be noted that the SERS effect in this study is a proof of field enhancement capability of the orderly structured metal foil with functional coating. With this capability, various applications based on light–matter interaction, such as nanophotonic devices and circuits, energy conversion devices, imaging, surface enhanced Raman scattering, and photothermal applications, could be pursued with suitable structural design in the future.

Patterning of hybrid films by LSI is demonstrated to be facile, rapid, economic, scalable and reproducible. Moreover, while most of the bottom-up patterning techniques involve several steps including chemical treatments, heat treatments *etc.*, top-down approaches suffer from reproducibility issues and pose an operational barrier for manufacturing of nano-

scale features. LSI provides a viable solution to such outstanding issues and is deemed to be a potential futuristic technology for precision manufacturing of functional nanoarchitectures. The present method exploits the excellent formability of aluminum metal and at the same time, gold surface coating provides plasmonic functionality to the printed 3D nanoshapes. Gold coating on the top of an aluminum foil can be replaced by other functional materials and thus one can attain 3D nanoshapes of desirable functional materials. The present experimental investigation thus gives rise to an innovative technology, capable of catering desired 3D nanoshapes with high precision as well as reproducibility in a scalable manner and with desired functionality.

4. Conclusion

In conclusion, gold arrays on flexible aluminum substrates have successfully been fabricated by laser induced shock pressure. Precise control over structural dimensions, ultrafast processing (nanosecond processing time), capability of roll-to-roll mass production at economic cost and in a scalable manner are some of the attributes of this emerging technology. The multi-layered deformation mechanism is investigated by developing a continuum model to study the induced stress wave propagation and temperature rise. The hybrid film treated by LSI shows improved surface smoothness, better interface and enhanced mechanical integrity for robust use. Patterned gold nanostructures act as an excellent optical antenna and results in strong optical field confinement, which have aptly been exploited for sensitive molecular detection. The cold processing nature of LSI would suit precision nano-manufacturing of functional structures on a variety of flexible substrates and thereby would find bio-applications. Since LSI is material wise versatile, it could provide ultrafast production of patterned functional nanofeatures laminated on flexible substrates with resolution beyond the limitations set by beam diffraction or scattering in conventional photolithography techniques, and has broad working window of various dimensions.

Acknowledgements

References

1 E. Ozbay, Plasmonics: merging photonics and electronics at nanoscale dimensions, *Science*, 2006, **311**, 189–193.

2   J. A. Schuller, E. S. Barnard, W. Cai, Y. C. Jun, J. S. White and M. L. Brongersma, Plasmonics for extreme light concentration and manipulation, *Nat. Mater.*, 2010, **9**, 193–204.

3   T. J. Echtermeyer, L. Britnell, P. K. Jasnos, A. Lombardo, R. V. Gorbachev, A. N. Grigorenko, A. K. Geim, A. C. Ferrari and K. S. Novoselov, Strong plasmonic enhancement of photovoltage in graphene, *Nat. Commun.*, 2011, **2**, 458.

4   C. Qian, C. Ni, W. Yu, W. Wu, H. Mao, Y. Wang and J. Xu, Highly-ordered, 3D petal-like array for surface-enhanced Raman scattering, *Small*, 2011, **7**, 1800–1806.

5   J. Henzie, M. H. Lee and T. W. Odom, Multiscale patterning of plasmonic metamaterials, *Nat. Nanotechnol.*, 2007, **2**, 549–554.

6   S. Lee, P. Kumar, Y. Hu, G. J. Cheng and J. Irudayaraj, Graphene laminated gold bipyramids as sensitive detection platforms for antibiotic molecules, *Chem. Commun.*, 2015, **51**, 15494–15497.

7   M. M. Hilali, S. Yang, M. Miller, F. Xu, S. Banerjee and S. V. Sreenivasan, Enhanced photocurrent in thin-film amorphous silicon solar cells via shape controlled three-dimensional nanostructures, *Nanotechnology*, 2012, **23**, 405203.

8   X. Zhang and Z. Liu, Superlenses to overcome the diffraction limit, *Nat. Mater.*, 2008, **7**, 435–441.

9   N. Fang, H. Lee, C. Sun and X. Zhang, Sub-diffraction-limited optical imaging with a silver superlens, *Science*, 2005, **308**, 534–537.

10 M. Mansuripur, A. R. Zakharian, A. Lesuffleur, S.-H. H. Oh, R. J. Jones, N. C. Lindquist, H. Im, A. Kobyakov and J. V. Moloney, Plasmonic nano-structures for optical data storage, *Opt. Express*, 2009, **17**, 14001–14014.

11 D. O'Connor and A. V. Zayats, Data storage: The third plasmonic revolution, *Nat. Nanotechnol.*, 2010, **5**, 482–483.

12 L. Pan and D. Bogy, Data storage: Heat-assisted magnetic recording, *Nat. Photonics*, 2009, **3**, 2–3.

13 K. Wang and K. B. Crozier, Plasmonic trapping with a gold nanopillar, *ChemPhysChem*, 2012, **13**, 2639–2648.

14 K. Wang, E. Schonbrun, P. Steinvurzel and K. B. Crozier, Trapping and rotating nanoparticles using a plasmonic nano-tweezer with an integrated heat sink, *Nat. Commun.*, 2011, **2**, 469.

15 L. Novotny, R. Bian and X. Xie, Theory of Nanometric Optical Tweezers, *Phys. Rev. Lett.*, 1997, **79**, 645–648.

16 B. J. Roxworthy, K. D. Ko, A. Kumar, K. H. Fung, E. K. C. Chow, G. L. Liu, N. X. Fang and K. C. Toussaint, Application of plasmonic bowtie nanoantenna arrays for optical trapping, stacking, and sorting, *Nano Lett.*, 2012, **12**, 796–801.

17 Commercializing plasmonics, *Nat. Photonics*, 2015, **9**, 477.

18 J. G. Ok, H. Seok Youn, M. Kyu Kwak, K.-T. Lee, Y. Jae Shin, L. Jay Guo, A. Greenwald and Y. Liu, Continuous and scalable fabrication of flexible metamaterial films via roll-to-roll nanoimprint process for broadband plasmonic infrared filters, *Appl. Phys. Lett.*, 2012, **101**, 223102.

19 L. T. Varghese, L. Fan, Y. Xuan, C. Tansarawiput, S. Kim and M. Qi, Resistless nanoimprinting in metal for plasmonic nanostructures, *Small*, 2013, **9**, 3778–3783.

20 S. Lee, M. G. Hahm, R. Vajtai, D. P. Hashim, T. Thurakitseree, A. C. Chipara, P. M. Ajayan and J. H. Hafner, Utilizing 3D SERS active volumes in aligned carbon nanotube scaffold substrates, *Adv. Mater.*, 2012, **24**, 5261–5266.

21 S. Lee, K. M. Mayer and J. H. Hafner, Improved localized surface plasmon resonance immunoassay with gold bipyramid substrates, *Anal. Chem.*, 2009, **81**, 4450–4455.

22 A. Van Blaaderen, R. Ruel and P. Wiltzius, Template-directed colloidal crystallization, *Nature*, 1997, 321–324.

23 M. Trau, N. Yao, E. Kim, Y. Xia, G. Whitesides and I. Aksay, Microscopic patterning of oriented mesoscopic silica through guided growth, *Nature*, 1997, **390**, 674–676.

24 J. P. Rolland, E. C. Hagberg, G. M. Denison, K. R. Carter and J. M. Simone, High-resolution soft lithography: enabling materials for nanotechnologies, *Angew. Chem., Int. Ed.*, 2004, **43**, 5796–5799.

25 G. Zhang, J. Zhang, G. Xie, Z. Liu and H. Shao, Cicada wings: a stamp from nature for nanoimprint lithography, *Small*, 2006, **2**, 1440–1443.

26 G. Kumar, H. X. Tang and J. Schroers, Nanomoulding with amorphous metals, *Nature*, 2009, **457**, 868–872.

27 M. C. McAlpine, R. S. Friedman and C. M. Lieber, Nanoimprint Lithography for Hybrid Plastic Electronics, *Nano Lett.*, 2003, **3**, 443–445.

28 S. Y. Chou, Nanoimprint lithography, *J. Vac. Sci. Technol., B: Microelectron. Nanometer Struct.-Process., Meas., Phenom.*, 1996, **14**, 4129.

29 B. D. Lucas, J.-S. Kim, C. Chin and L. J. Guo, Nanoimprint Lithography Based Approach for the Fabrication of Large-Area, Uniformly-Oriented Plasmonic Arrays, *Adv. Mater.*, 2008, **20**, 1129–1134.

30 L. J. Guo, Nanoimprint Lithography: Methods and Material Requirements, *Adv. Mater.*, 2007, **19**, 495–513.

31 X. Zhu, Y. Zhang, J. Zhang, J. Xu, Y. Ma, Z. Li and D. Yu, Ultrafine and smooth full metal nanostructures for plasmonics, *Adv. Mater.*, 2010, **22**, 4345–4349.

32 S. Cherukulappurath, T. W. Johnson, N. C. Lindquist and S.-H. Oh, Template-stripped asymmetric metallic pyramids for tunable plasmonic nanofocusing, *Nano Lett.*, 2013, **13**, 5635–5641.

33 K. L. Lee, P. W. Chen, S. H. Wu, J. B. Huang, S. Y. Yang and P. K. Wei, Enhancing surface plasmon detection using template-stripped gold nanoslit arrays on plastic films, *ACS Nano*, 2012, **6**, 2931–2939.

34 P. Nagpal, N. C. Lindquist, S.-H. Oh and D. J. Norris, Ultrasmooth patterned metals for plasmonics and metamaterials, *Science*, 2009, **325**, 594–597.

35 G. Kumar, H. X. Tang and J. Schroers, Nanomoulding with amorphous metals, *Nature*, 2009, **457**, 868–872.

36 X. Liu, Y. Shao, Y. Tang and K.-F. Yao, Highly uniform and reproducible surface enhanced Raman scattering on air-stable metallic glassy nanowire array, *Sci. Rep.*, 2014, **4**, 5835.

37 Y. Hu, S. Lee, P. Kumar, Q. Nian, W. Wang, J. J. Irudayaraj and G. J. Cheng, Water flattens graphene wrinkles: laser shock wrapping of graphene onto substrate-supported

crystalline plasmonic nanoparticle arrays, *Nanoscale*, 2015, **7**, 19885–19893.

38 G. Huang, Y. Hu, Y. Xuan, J. Li, Y. Yang, R. V. Martinez, C. Li, J. Luo, M. Qi and G. J. Cheng, Large-scale nanoshaping of ultrasmooth 3D crystalline metallic structures, *Science*, 2014, **346**(6215), 1352–1356.

39 P. Kumar, J. Li, Q. Nian, Y. Hu and G. J. Cheng, Plasmonic tuning of silver nanowires by laser shock induced lateral compression, *Nanoscale*, 2013, **5**, 6311–6317.

40 W. C. Oliver and G. M. Pharr, An improved technique for determining hardness and elastic modulus using load and displacement sensing indentation experiments, *J. Mater. Res.*, 1992, **7**, 1564–1583.

41 W. Logan, A. Agrawal, K. M. Flores and W. Windl, Rapid Production of Accurate Embedded-Atom Method Potentials for Metal Alloys, 2012, arXiv:1209.0619.

42 J. Li, H. Gao and G. J. Cheng, Forming Limit and Fracture Mode of Microscale Laser Dynamic Forming, *J. Manuf. Sci. Eng.*, 2010, **132**, 061005.

43 E. Pierazzo, N. Artemieva, E. Asphaug, E. C. Baldwin, J. Cazamias, R. Coker, G. S. Collins, D. A. Crawford, T. Davison, D. Elbeshausen, K. A. Holsapple, K. R. Housen, D. G. Korycansky and K. Wünnemann, Validation of numerical codes for impact and explosion cratering: Impacts on strengthless and metal targets, *Meteorit. Planet. Sci.*, 2008, **43**, 1917–1938.

44 R. Fabbro, J. Fournier, P. Ballard, D. Devaux and J. Virmont, Physical study of laser-produced plasma in confined geometry, *J. Appl. Phys.*, 1990, **68**, 775–784.

45 H. Gao, C. Ye and G. J. Cheng, Deformation Behaviors and Critical Parameters in Microscale Laser Dynamic Forming, *J. Manuf. Sci. Eng.*, 2009, **131**, 051011.

46 Y. Liao, S. Suslov, C. Ye and G. J. Cheng, The mechanisms of thermal engineered laser shock peening for enhanced fatigue performance, *Acta Mater.*, 2012, **60**, 4997–5009.

47 C. Ye, S. Suslov, D. Lin and G. J. Cheng, Deformation-induced martensite and nanotwins by cryogenic laser shock peening of AISI 304 stainless steel and the effects on mechanical properties, *Philos. Mag.*, 2012, **92**, 1369–1389.

48 Y. Liao, Y. Yang and G. J. Cheng, Enhanced Laser Shock by an Active Liquid Confinement—Hydrogen Peroxide, *J. Manuf. Sci. Eng.*, 2012, **134**, 034503.

49 Y. Liao, C. Ye, H. Gao, B.-J. Kim, S. Suslov, E. A. Stach and G. J. Cheng, Dislocation pinning effects induced by nanoprecipitates during warm laser shock peening: Dislocation dynamic simulation and experiments, *J. Appl. Phys.*, 2011, **110**, 023518.

50 H. Gao, C. Ye and G. J. Cheng, Deformation Behaviors and Critical Parameters in Microscale Laser Dynamic Forming, *J. Manuf. Sci. Eng.*, 2009, **131**, 051011.

51 K. Jonnalagadda, N. Karanjgaokar, I. Chasiotis, J. Chee and D. Peroulis, Strain rate sensitivity of nanocrystalline Au films at room temperature, *Acta Mater.*, 2010, **58**, 4674–4684.

52 N. J. Karanjgaokar, C. S. Oh, J. Lambros and I. Chasiotis, Inelastic deformation of nanocrystalline Au thin films as a function of temperature and strain rate, *Acta Mater.*, 2012, **60**, 5352–5361.

53 T. Zhang, W. Xu and M. Zhao, The role of plastic deformation of rough surfaces in the size-dependent hardness, *Acta Mater.*, 2004, **52**, 57–68.

54 Y. Huang, F. Zhang, K. C. Hwang, W. D. Nix, G. M. Pharr and G. Feng, A model of size effects in nano-indentation, *J. Mech. Phys. Solids*, 2006, **54**, 1668–1686.

55 A. Gouldstone, K. J. Van Vliet and S. Suresh, Nanoindentation. Simulation of defect nucleation in a crystal, *Nature*, 2001, **411**, 656.

56 D. Lorenz, A. Zeckzer, U. Hilpert, P. Grau, H. Johansen and H. Leipner, Pop-in effect as homogeneous nucleation of dislocations during nanoindentation, *Phys. Rev. B: Condens. Matter*, 2003, **67**, 1–4.

57 J. R. Morris, H. Bei, G. M. Pharr and E. P. George, Size effects and stochastic behavior of nanoindentation pop in, *Phys. Rev. Lett.*, 2011, **106**, 1–4.

58 X. Zhu, L. Shi, M. S. Schmidt, A. Boisen, O. Hansen, J. Zi, S. Xiao and N. A. Mortensen, Enhanced light-matter interactions in graphene-covered gold nanovoid arrays, *Nano Lett.*, 2013, **13**, 4690–4696.